Feasibility of similarity coefficient map for improving morphological evaluation of T_2^* weighted MRI for renal cancer*

Wang Hao-Yu(王浩宇)[a], Hu Jiani[b], Xie Yao-Qin(谢耀钦)[c], Chen Jie(陈 杰)[d], Yu Amy[e], Wei Xin-Hua(魏新华)[f], Dai Yong-Ming(戴勇鸣)[g], Li Meng[b], Bao Shang-Lian(包尚联)[a]†, and E. M. Haacke[b]

[a] *Beijing Key Laboratory of Medical Physics and Engineering, Peking University, Beijing* 100871, *China*
[b] *Department of Radiology, Wayne State University, Detroit* 48201, *USA*
[c] *Chinese Academy of Sciences, Key Laboratory of Health Information , Institute of Advanced Technology, Shenzhen* 518055, *China*
[d] *Changzhou First People's Hospital, Changzhou* 213003, *China*
[e] *College of Literature Science and the Arts, University of Michigan, Ann Arbor, Michigan* 48103, *USA*
[f] *Department of Radiology, Guangzhou First Municipal People's Hospital, Guangzhou* 510180, *China*
[g] *Siemens Healthcare China, MR Collaboration NE Asia, Shanghai* 210318, *China*

(Received 19 September 2012; revised manuscript received 13 November 2012)

The purpose of this paper is to investigate the feasibility of using a similarity coefficient map (SCM) in improving the morphological evaluation of T_2^* weighted (T_2^*W) magnatic resonance imaging (MRI) for renal cancer. Simulation studies and *in vivo* 12-echo T_2^*W experiments for renal cancers were performed for this purpose. The results of the first simulation study suggest that an SCM can reveal small structures which are hard to distinguish from the background tissue in T_2^*W images and the corresponding T_2^* map. The capability of improving the morphological evaluation is likely due to the improvement in the signal-to-noise ratio (SNR) and the carrier-to-noise ratio (CNR) by using the SCM technique. Compared with T_2^*W images, an SCM can improve the SNR by a factor ranging from 1.87 to 2.47. Compared with T_2^* maps, an SCM can improve the SNR by a factor ranging from 3.85 to 33.31. Compared with T_2^*W images, an SCM can improve the CNR by a factor ranging from 2.09 to 2.43. Compared with T_2^* maps, an SCM can improve the CNR by a factor ranging from 1.94 to 8.14. For a given noise level, the improvements of the SNR and the CNR depend mainly on the original SNRs and CNRs in T_2^*W images, respectively. *In vivo* experiments confirmed the results of the first simulation study. The results of the second simulation study suggest that more echoes are used to generate the SCM, and higher SNRs and CNRs can be achieved in SCMs. In conclusion, an SCM can provide improved morphological evaluation of T_2^*W MR images for renal cancer by unveiling fine structures which are ambiguous or invisible in the corresponding T_2^*W MR images and T_2^* maps. Furthermore, in practical applications, for a fixed total sampling time, one should increase the number of echoes as much as possible to achieve SCMs with better SNRs and CNRs.

Keywords: renal cancer, T_2^* weighted MRI, similarity coefficient map

PACS: 87.61.−c, 87.57.C−

DOI: 10.1088/1674-1056/22/3/038702

1. Introduction

In the US, about 65000 incidences of renal cancer are estimated to have been diagnosed in 2012, making it one of the most common type of cancer.[1] Fortunately, the 5-year survival rate for patients with renal cancer is increasing. This is partly due to the implementation of non-invasive medical imaging techniques including magnetic resonance imaging (MRI) which helps in the detection of renal cancers at an early stage.[2]

MRI is an extensively used non-invasive medical imaging technique which utilizes the property of nuclear magnetic resonance (NMR) to image water protons inside a human body. The MRI technique has long been used in renal cancer detection,[3–6] preoperative renal cancer staging,[7–12] and treatment evaluation of renal cancers.[13]

Among a variety of MR techniques, T_2^* weighted (T_2^*W) MRI has been used to reveal not only functional but also morphological characteristics of renal diseases by taking advantage of differences in tissue properties such as the blood oxygen level and magnetic susceptibility. For example, Prasad *et al.* have implemented T_2^*W blood-oxygen-level-dependent (BOLD) MRI to evaluate the level of oxygenation in kidneys.[14] Tanaka *et al.* have proposed that T_2^*W MRI is superior in the detection of hemosiderin in the kidney because it is more sensitive to susceptibility effects.[15]

Although the quality of MRI is excellent in general, there is always room for further improvement. The quality of MR images can directly determine the accuracy of clinical diagnosis of renal cancers, particularly when detailed morphological characteristics of tissues are required. For example, morphological characteristics of hemorrhages[16,17] and pseudocapsules[18–21] are both important for the diagnosis, treatment planning and prognosis of renal can-

*Project supported by the National Basic Research Program of China (Grant No. 2011CB707701) and the National Key Technology R&D Program of China (Grant Nos. 2011BAI12B05 and 2012BAI23B07).

†Corresponding author. E-mail: bao@pku.edu.cn

© 2013 Chinese Physical Society and IOP Publishing Ltd

cers. Thus, constant efforts have been made to improve the quality of MR images, including the development of post-processing techniques,[22–25] optimization of the scanning parameters,[26–29] and purchase of expensive high-field MR scanners.[30–34]

A tissue similarity map (TSM) is a post-processing method designed to show the relatedness of the tissue of interest and the reference tissue with a high contrast-to-noise ratio (CNR) and a high signal-to-noise ratio (SNR).[35–37] However, it is sensitive to the choice of reference tissue, which makes it unsuitable for the purpose of improving the morphological evaluation of multi-echo T_2^*W MR images. Recently, the λ map, which is derived from a TSM and insensitive to the choice of reference tissue, has been proposed to demonstrate the hemodynamic characteristics of brain tissues with a high SNR.[37] Inspired by the idea of the λ map, a similarity coefficient map (SCM) has been proposed in this paper for the purpose of improving the morphological evaluation of multi echo T_2^*W MR images for renal cancer. The main objective of this paper is to investigate the feasibility of SCMs in improving the evaluation of the morphological characteristics of renal cancer. The effects of the number of echoes on an SCM are also evaluated. To accomplish these objectives, a simulation study and *in vivo* experiments are performed. Simulation studies aim to provide theoretical support for the feasibility of using SCMs to improve the morphological evaluation of T_2^*W MR images for the kidney, and *in vivo* experiments are performed to verify the results.

2. Method and material

2.1. Similarity coefficient map

TSMs have been proposed to demonstrate the relatedness of a tissue of interest and the reference tissue by taking advantage of the mean squared error (MSE) between them. For multi-echo T_2^*W imaging, the MSE between a tissue of interest and the reference tissue can be given by[35,36]

$$\mathrm{MSE}(\boldsymbol{r}) = \frac{1}{N}\sum_{i=1}^{N}(S_i(\boldsymbol{r}) - S_{\mathrm{ref},i})^2, \tag{1}$$

where $\boldsymbol{r}$ denotes the location of the tissue of interest, i denotes the index of a T_2^*W image in the acquisition series, N denotes the total number of T_2^*W images, S_i and $S_{\mathrm{ref},i}$ denote the signal intensity of the tissue of interest, and the reference tissue in the i-th ($i = 1,2,\ldots,N$) T_2^*W image, respectively.

However, a TSM is sensitive to the choice of reference tissue, which makes it unsuitable for improving the morphological evaluation of multi-echo T_2^*W MR images. As shown in Appendix, if the reference tissue is not properly selected, a TSM may have a problem in identifying two tissues that have different characteristics (see Fig. A1(c)). To overcome this problem, a similarity coefficient map (SCM), which is less sensitive to the choice of reference tissue (see Appendix), has been proposed in this paper.

The basic idea of an SCM is similar to the λ map, which is insensitive to the choice of reference tissue and has been designed to demonstrate the hemodynamic characteristics of brain tissues with a high SNR.[37] However, the SCM proposed in this paper is specifically designed for the purpose of improving the morphological evaluation of multi-echo T_2^*W MR images. The derivation of an SCM is given as follows. First, a similarity coefficient α is introduced into Eq. (1)

$$\mathrm{MSE}_\alpha(\boldsymbol{r}) = \frac{1}{N}\sum_{i=1}^{N}(S_i(\boldsymbol{r}) - \alpha(\boldsymbol{r})S_{\mathrm{ref},i})^2. \tag{2}$$

Then, α determining the minimum MSE_α can be found by the following equation:

$$\alpha(\boldsymbol{r}) = \frac{\sum_{i=1}^{N} S_i(\boldsymbol{r})S_{\mathrm{ref},i}}{\sum_{i=1}^{N} S_{\mathrm{ref},i}S_{\mathrm{ref},i}}. \tag{3}$$

Equation (3) is the definition of the SCM.

2.2. Simulation studies

Simulation studies were conducted to investigate the theoretical basis of the SCM technique. The first simulation study was designed to examine the improvement of the morphological evaluation of an SCM compared with the T_2^*W images and the corresponding T_2^* maps. The second simulation study was designed to evaluate the effects of the number of echoes N on an SCM.

A digital phantom designed for multi-echo T_2^*W imaging was created (see Fig. 1(a)). It consisted of an ellipse representing the renal parenchyma (tissue 1 with longest $T_2^* = 60$ ms), and two series of small solid circles with different radii (from left to right: 1, 2, 4, 8, and 16 pixels, respectively). The small solid circles in the upper series represent tissue 2, which has a medium T_2^* (40 ms). The small solid circles in the bottom series represent tissue 3, which has the shortest T_2^* (20 ms). Outside the phantom was air circumstance, which was supposed to provide nothing but pure noise.

2.2.1. The improvement of morphological evaluation

The first simulation study was designed to examine the improvement of the morphological evaluation of the SCM. A series of 12-echo T_2^*W MR images were simulated with the echo time (T_E) ranging from 2 ms to 24 ms (at an equal time interval of 2 ms) using a fast low angle shot (FLASH) pulse sequence. The digital phantom described at the beginning of section 2.2 was used in this simulation. Assuming that the flip angle was small, the signal intensity of the FLASH pulse sequence was given by $I_s\ (T_\mathrm{E}) = \rho\exp(-T_\mathrm{E}/T_2^*)$,[38] where ρ was a constant of relative proton density which was set to be 1.

Rician noise at different levels (4%, 8%, and 16%) were introduced in the simulated T_2^*W images by adding white Gaussian noise N (0, σ^2) to real and imaginary channels, respectively, as described in previous work.[39] The levels of Rician noise were determined by the levels of Gaussian noise. For example, 4% Rician noise means that the standard deviation (SD) of the Gaussian noise was $\sigma = 4\%I_{\max}$, where $I_{\max}$ was the maximum signal intensity of all T_2^*W images.

SCMs were generated from the multi-echo T_2^*W images with different noise levels (4%, 8%, and 16%). Since the multi-echo T_2^*W images were available, it was easy to obtain the corresponding T_2^* map which can be used to identify lesions from normal tissues by demonstrating the functional characteristics of the different tissues.[40,41] Thus, corresponding T_2^* maps were also generated by fitting a mono exponential model[42] for comparison purposes.

To test the ability of an SCM in improving morphological evaluation, SNRs and CNRs of simulated T_2^*W images, the corresponding SCMs, and T_2^* maps were compared for each tissue and each noise level as follows. First, for each tissue, the SNR was calculated as the ratio of the mean signal intensities of the tissue to the standard deviation of the tissue. CNRs of different pairs of tissues (tissues 1 and 2; tissues 1 and 3) were calculated using $|I_{\text{tis}} - I_{\text{ref}}|/\sqrt{D_{\text{tis}}^2 + D_{\text{ref}}^2}$,[43] where I_{tis} and I_{ref} denote the mean signal intensities of the tissue of interest (tissue 2 or tissue 3) and the reference tissue (tissue 1), respectively. D_{tis} and D_{ref} denote the standard deviation of the tissue of interest and the reference tissue, respectively. Second, for each tissue (or each pair of tissues) and each noise level, the $\text{SNR}_{\max}$ (or $\text{CNR}_{\max}$) of the simulated T_2^*W images that have maximum SNRs (or CNRs) and $\text{SNR}_{\text{T2*map}}$ (or $\text{CNR}_{\text{T2*map}}$) of T_2^* maps were compared with the SNR_{SCM} (or CNR_{SCM}) of corresponding SCMs in terms of the improvement factor $R = \text{SNR}_{\text{SCM}}/\text{SNR}_{\max}$ (or $R = \text{CNR}_{\text{SCM}}/\text{CNR}_{\max}$) for the comparison of the SCM and T_2^*W images, and $R = \text{SNR}_{\text{SCM}}/\text{SNR}_{\text{T2*map}}$ (or $R = \text{CNR}_{\text{SCM}}/\text{CNR}_{\text{T2*map}}$) for the comparison of the SCM and T_2^* map.

2.2.2. The effects of the number of echoes N on the SCM

The second simulation study was designed to evaluate the effects of the number of echoes (N) on an SCM. The simulation was conducted as follows. First, let T_{a} be the total sampling time, which was defined as $T_{\text{a}} = NT_{\text{s}}$, where N denotes the number of echoes and T_{s} denotes the sampling period of a single echo. For a multi-echo T_2^*W FLASH pulse sequence, T_{a} was determined by the repetition time T_{R} and the time periods of the other waveforms of pulse sequence T_{other}, i.e., $T_{\text{a}} = T_{\text{R}}$-$T_{\text{other}}$. For a given T_{R} and a fixed T_{other}, T_{a} should be a constant which was set to be $T_{\text{a}} = 24$ ms in this simulation study. Second, for a given T_{a}, the number of echoes N is determined by $N = T_{\text{a}}/T_{\text{s}}$. Three series of multi-echo T_2^*W MR images were simulated with different N (3, 6, and 12, respectively) and corresponding T_{s} (8 ms, 4 ms, and 2 ms, respectively). Third, for a given N and the corresponding T_{s}, the initial echo time τ was considered to satisfy the following equation, $\tau = T_{\text{s}}/2$. Figure 1 shows the definition of time periods of the multi-echo T_2^*W imaging pulse sequence implemented in this simulation study. As shown in Fig. 1, the sampling time period of a single echo was $T_{\text{s}} = 2(\tau - \tau_0)$, where τ denotes the initial echo time, and τ_0 denotes the time period from excitation RF pulse to the start of the first sampling period. For the convenience of calculation, τ_0 was considered to be much shorter than the initial echo time and can be omitted in this simulation study. Therefore, we have $\tau = T_{\text{s}}/2$. Fourth, for each series of multi-echo T_2^*W MR images, assuming a symmetric sampling of echoes was used (see Fig. 1), the i-th echo time $T_{\text{E}i} = (2i-1)\tau$, where i was the index of the echoes ($i = 1, 2, \ldots, N$). In addition, it is well known that by keeping other scanning parameters unchanged, the standard deviation of noise σ is proportional to the square root of the receiver bandwidth BW, which is inversely proportional to T_{s}.[38] Thus, σ was assumed to be proportional to $1/\sqrt{T_{\text{s}}}$. According to the definition of noise level described in Section 2.2.1, the noise level was also proportional to $1/\sqrt{T_{\text{s}}}$. Therefore, if the noise level in the case that $T_{\text{s}} = 2$ ms ($N = 12$) was set to be 16%, the noise levels in the cases that $T_{\text{s}} = 4$ ms ($N = 6$) and $T_{\text{s}} = 8$ ms ($N = 3$) were $8\sqrt{2}\%$ and 8%, respectively. The digital phantom described at the beginning of Section 2.1 was used in this simulation experiment. The signal intensity of the FLASH pulse sequence was given by $I_{\text{s}}(T_{\text{E}}) = \rho \exp(-T_{\text{E}}/T_2^*)$, where ρ was the relative proton density, which was set to be 1. Table 1 lists the parameters implemented in the three series of multi-echo T_2^*W imaging in this simulation study.

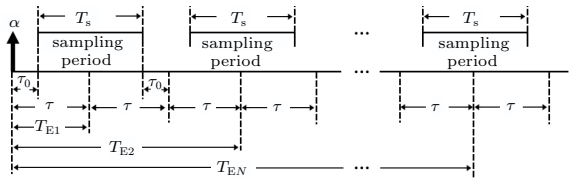


Fig. 1. Definition of the time periods of the multi-echo T_2^*W imaging pulse sequence implemented in the second simulation study, which is designed to evaluate the effects of N on SCM.

SCMs were generated from the three series of multi-echo T_2^*W images which have different number of echoes ($N = 3$, 6, and 12), respectively. The SNRs and CNRs of SCMs generated from different numbers of echoes were compared with each other.

Table 1. Parameters of the three series of the multi-echo T_2^*W imaging pulse sequence implemented in the second simulation study which is designed to evaluate the evaluate the effects of N on the SCM.

Index of series	N	T_{s}/ms	τ/ms	Noise level
1	3	8	4	8%
2	6	4	2	$8\sqrt{2}\%$
3	12	2	1	16%

2.3. *In vivo* SCM of a T_2^*W MRI for renal cancer

SCMs generated from *in vivo* 12-echo T_2^*W images of renal cancers were compared with the corresponding T_2^*W images and T_2^* maps to test the feasibility of using SCMs in providing an improved morphological evaluation of renal cancers. Written consent forms were obtained from all patients ($N = 2$) and approved by the Human Investigation Committee at the participating institution. Corresponding T_2^* maps were generated by fitting a mono exponential model for the purpose of comparison. In addition, the relative proton density (RPD) values of tissues of interest were estimated by fitting a mono exponential model[42] to evaluate the consistency of the *in vivo* experiment and the first simulation study.

The *in vivo* multi-echo T_2^*W images of patients with renal cancers were acquired on a 3T MRI scanner (Vario, Siemens, Germany) using an FLASH pulse sequence with the following parameters: 12 echoes with T_E ranging from 2.35 ms to 24.13 ms with an equal interval of 1.98 ms, $T_R = 162$ ms, flip angle of 15°, matrix size of 288×384, field of view: 285×380 mm^2, and slice thickness of 5 mm.

For the two patients involved in the *in vivo* experiment, the morphological characteristics of hemorrhages and pseudocapsules were examined, respectively. For each patient, the SCM was generated with the normal renal parenchyma of the patient as the reference tissue.

SNRs and CNRs were calculated to explore the reason behind the SCM in improving morphological evaluation. First, ROIs were selected by experienced clinical doctors in normal renal parenchyma (for each patient), hemorrhage (for patient #1), and pseudocapsule (for patient #2), respectively. Then, for each ROI, the SNR was calculated as the ratio of the mean signal intensities of the ROI to the standard deviation (SD) of the ROI. CNRs of different pairs of tissues (hemorrhage-normal renal parenchyma, and pseudocapsule-normal renal parenchyma) were calculated using $I_{tis} - I_{ref}|/\sqrt{D_{tis}^2 + D_{ref}^2}$,[43] where I_{tis} and I_{ref} denote the mean signal intensities of the tissue of interest and the reference tissue, respectively, and D_{tis} and D_{ref} denote the standard deviation of tissue of interest and the reference tissue, respectively. Finally, for each tissue (or each pair of tissues), the SNR_{max} (or CNR_{max}) of the original T_2^*W images that have a maximum SNR (or CNR) and SNR_{T2*map} (or CNR_{T2*map}) of the T_2^* maps were compared with the SNR_{SCM} (or CNR_{SCM}) of corresponding SCMs in terms of the improvement factor R as described in Section 2.2.1.

3. Results

3.1. Simulation experiments

3.1.1. The improvement of morphological evaluation

Figure 2 shows a comparison of the noise corrupted T_2^*W images (4%, 8%, and 16% noise), the corresponding T_2^* maps, and the SCMs. Figure 2(a) shows the digital phantom designed for the simulation experiment of kidney imaging as described in Section 2.2. Figures 2(b)–2(e), 2(h)–2(k), and 2(n)–2(q) are representative simulated T_2^*W images with $T_E = 2$, 8, 14, and 20 ms at noise levels of 4%, 8%, and 16%, respectively. Figures 2(f), 2(l), and 2(r) are the corresponding T_2^* maps. Figures 2(g), 2(m), and 2(s) are the corresponding SCMs generated from the simulated T_2^*W images at noise levels of 4%, 8%, and 16%, respectively. White arrows indicate fine structures of the digital phantoms for comparison.

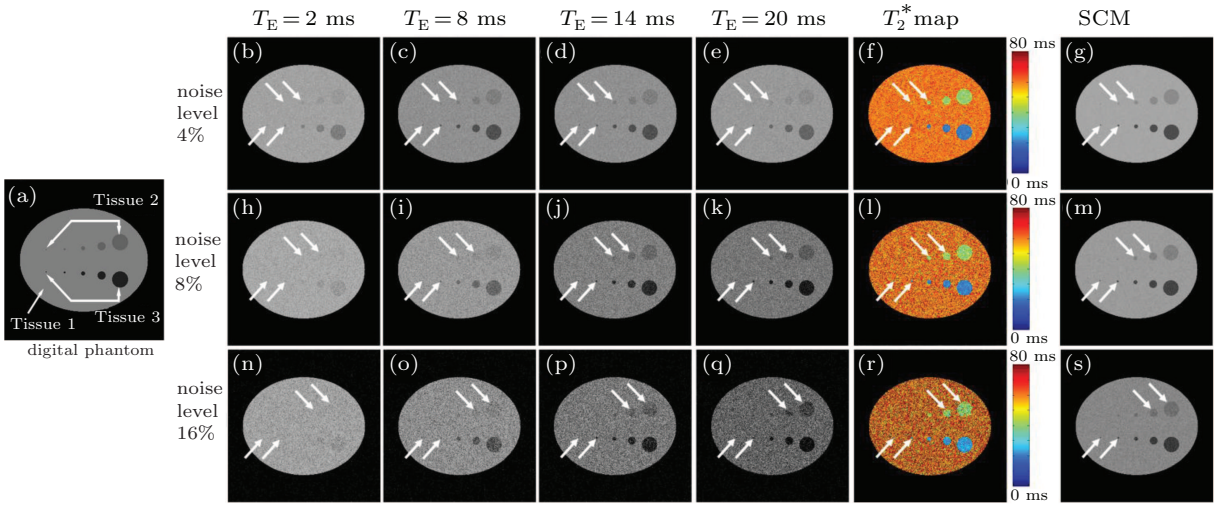


Fig. 2. (color online) A comparison of noise corrupted T_2^*W images (4%, 8%, and 16% noise), T_2^* maps, and the corresponding SCMs. (a) Digital phantom designed for the simulation experiments. The phantom consists of an ellipse which represents the renal parenchyma (tissue 1 with longest T_2^* of 60 ms), and two series of small circles with different radii (from left to right: 1, 2, 4, 8, and 16 pixels, respectively). The small solid circles in the upper series represent tissues that have the medium T_2^* of 40 ms. The small circles in the bottom series represent tissues that have a shortest T_2^* of 20 ms. Outside the phantom is the air circumstance which is supposed to provide nothing but pure noise. (b)–(e), (h)–(k), and (n)–(q) show representative T_2^*W images of multi-echo T_2^*W imaging with $T_E = 2$, 8, 14, and 20 ms at noise levels of 4%, 8%, and 16%, respectively. (f), (l), and (r) show corresponding T_2^* maps. (g), (m), and (s) are the SCMs generated from the T_2^*W images at noise levels of 4%, 8%, and 16%, respectively. White arrows indicate some fine structures of the digital phantoms for comparison.

Figure 3 shows the SNRs (and CNRs) of the simulated T_2^*W images and T_2^* maps, together with the corresponding SCMs at different noise levels for comparison. In Figs. 3(a)–3(c), we compare the SNRs of all tissues (tissue 1, tissue 2, and tissue 3) in simulated T_2^*W images that have maximum SNRs (indicated by dotted bars), T_2^* maps (slashed bars), and SCMs (solid black bars) at noise levels of 4%, 8%, and 16%, respectively. The horizontal axis shows different tissues and the longitude axis shows the SNR. In Figs. 3(d)–3(f), we compare the CNRs of different pairs of tissues (tissues 1 and 2, tissues 1 and 3) in simulated T_2^*W images that have maximum CNRs (indicated by dotted bars), T_2^* maps (slashed bars), and SCMs (solid black bars) at noise levels of 4%, 8%, and 16%, respectively. The horizontal axis shows different pairs of tissues used to calculate the CNRs, and the longitudinal axis shows the CNR.

In Fig. 4, we compare the improvement of the SNRs (and CNRs) of different tissues (and pairs of tissues) at different noise levels (4%, 8%, and 16%). Figures 4(a)–4(c) illustrate the comparison of improvement factors of the SNRs of different tissues (tissue 1, tissue 2, and tissue 3) at different noise levels (4%, 8%, and 16%, respectively). The improvement

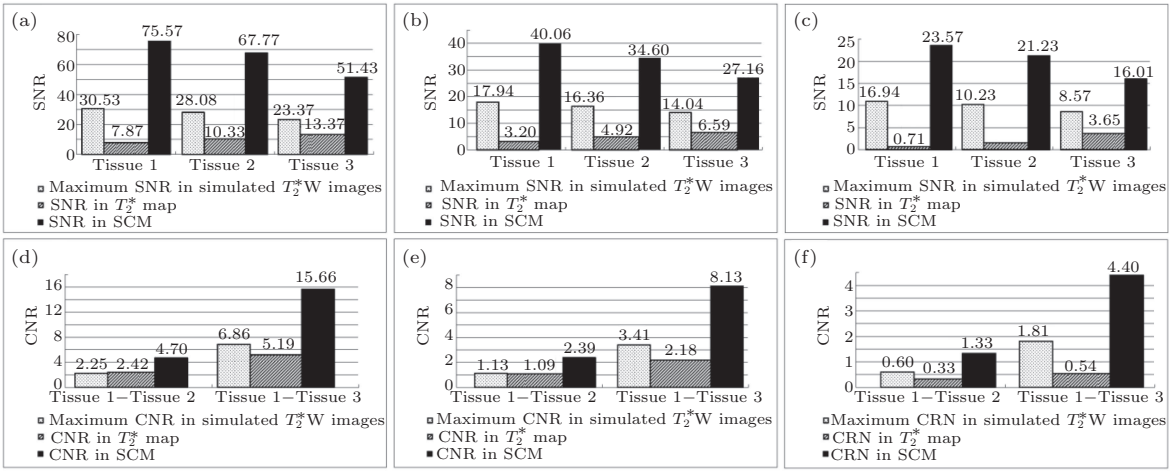


Fig. 3. A comparison of SNRs (and CNRs) of the simulated T_2^*W images,T_2^* maps, and the corresponding SCMs at different noise levels. (a)–(c) Comparison of the SNRs of all tissues (tissue 1, tissue 2, and tissue 3) in simulated T_2^*W images that have maximum SNRs (indicated by dotted bars),T_2^* maps (slashed bars), and SCMs (solid black bars) at noise levels of 4%, 8%, and 16%, respectively. The horizontal axis shows different tissues and the longitude axis shows SNR. (d)–(f) Comparison of the CNRs of different pairs of tissues (tissues 1 and 2, tissues 1 and 3) in simulated T_2^*W images that have maximum CNRs (dotted bars),T_2^* maps (slashed bars), and SCMs (solid black bars) at noise levels of 4%, 8%, and 16%, respectively. The horizontal axis shows different pairs of tissues used to calculate the CNRs, and the longitudinal axis shows the CNR.

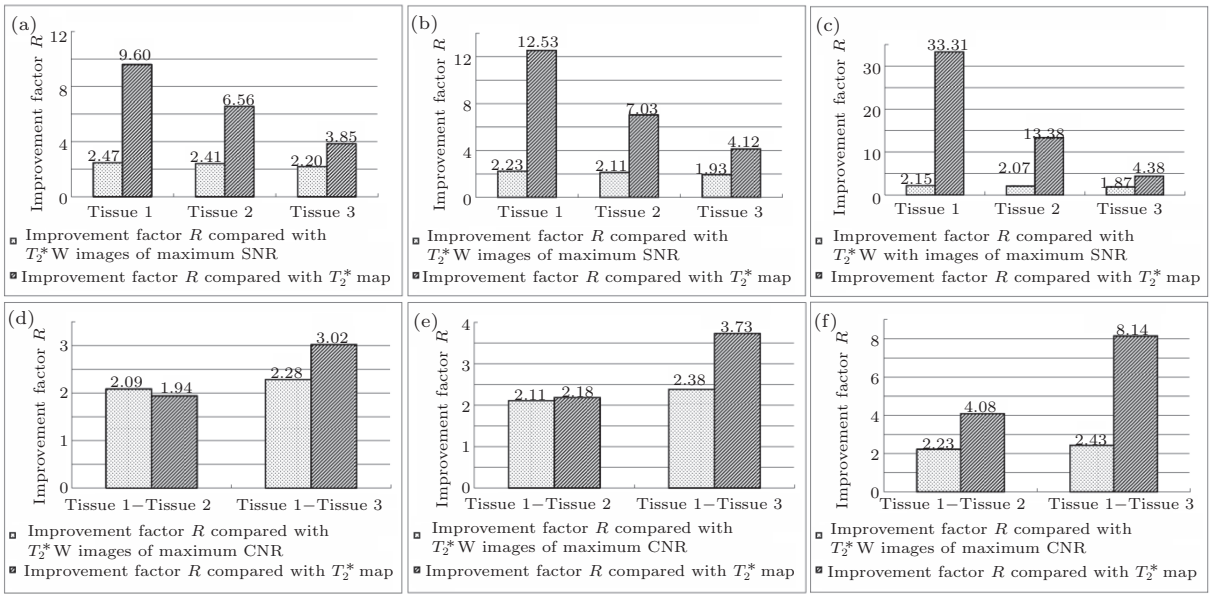


Fig. 4. A comparison of the improvement of SNRs (and CNRs) of different tissues (and pairs of tissues) at different noise levels (4%, 8%, and 16%). (a)–(c) Comparison of the improvement of SNRs of different tissues (tissue 1, tissue 2, and tissue 3) at different noise levels (4%, 8%, and 16%). The improvement factor R of the SNR relative to T_2^*W images of maximum SNR and the T_2^* maps are indicated by dotted bars and slashed bars, respectively. The horizontal axis shows different tissues and the longitude axis shows the improvement factor R of SNR. (d)–(f) Comparison of the improvement of the CNRs of different pairs of tissues (tissues 1 and 2, tissues 1 and 3) at different noise levels (4%, 8%, and 16%). The improvement factor R of the CNR relative to T_2^*W images of the maximum CNR and the T_2^* maps are indicated by dotted bars and slashed bars, respectively. The horizontal axis shows different pairs of tissues and the longitudinal axis shows the improvement factor R of CNR.

factors R of the SNR relative to T_2^*W images of the maximum SNR and the T_2^* maps are indicated by dotted bars and slashed bars, respectively. The horizontal axis shows different tissues and the longitude axis shows the improvement factor R of SNR. Figures 4(d)–4(f) illustrate the comparison of improvement of CNRs of different pairs of tissues (tissues 1 and 2, tissues 1 and 3) at different noise levels (4%, 8%, and 16%). The improvement factors R of the CNR relative to T_2^*W images of the maximum CNR and the T_2^* maps are indicated by dotted bars and slashed bars, respectively. The horizontal axis shows different pairs of tissues and the longitudinal axis shows the improvement factor R of CNR.

3.1.2. The effects of the number of echoes N on the SCM

Figure 5(a) shows the SNRs in SCMs generated with different numbers of echoes ($N = 3, 6, 12$). Figure 5(b) shows the CNRs in SCMs generated with different numbers of echoes ($N = 3, 6, 12$).

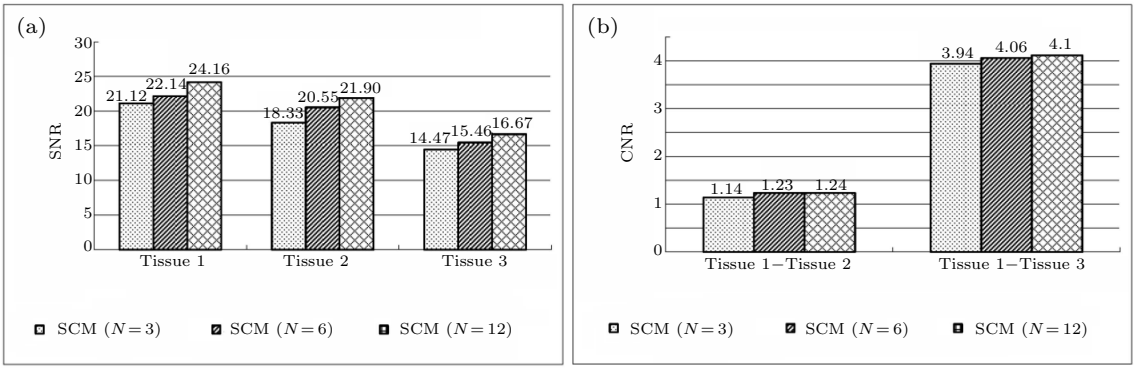


Fig. 5. A comparison of SNRs and CNRs in SCMs generated with different numbers of echoes. (a) SNRs of different tissues in SCMs generated with different numbers of echoes ($N = 3, 6, 12$). (b) CNRs of different pairs of tissues in SCMs generated with different numbers of echoes ($N = 3, 6, 12$).

3.2. *In vivo* SCM of T_2^*W kidney MRI

In Fig. 6, we compare *in vivo* T_2^*W images, the T_2^* map, and the corresponding SCM of patient #1 who has renal cancer with hemorrhaging. Figures 6(a)–6(d) shows the representative *in vivo* T_2^*W images at T_E of 2.35 ms, 8.29 ms, 14.23 ms, and 20.17 ms, respectively. Figure 6(e) shows the corresponding T_2^* map. Figure 6(f) shows the corresponding SCM generated with normal renal parenchyma as the reference tissue. The white arrows indicate the locations of several dot-like hemorrhages in renal cancer.

In Fig. 7, we compare *in vivo* T_2^*W images, T_2^* map, and the corresponding SCMs of patient #2 who has a renal tumor with a pseudocapsule. Figures 7(a)–7(d) shows the representative *in vivo* T_2^*W images at T_E of 2.35 ms, 8.29 ms, 14.23 ms, and 20.17 ms, respectively. Figure 7(e) shows the corresponding T_2^* map. Figure 7(f) shows the corresponding SCM generated with a normal renal parenchyma as the reference tissue. The solid white arrows indicate the pseudocapsule (region of hypointense) of the renal tumor.

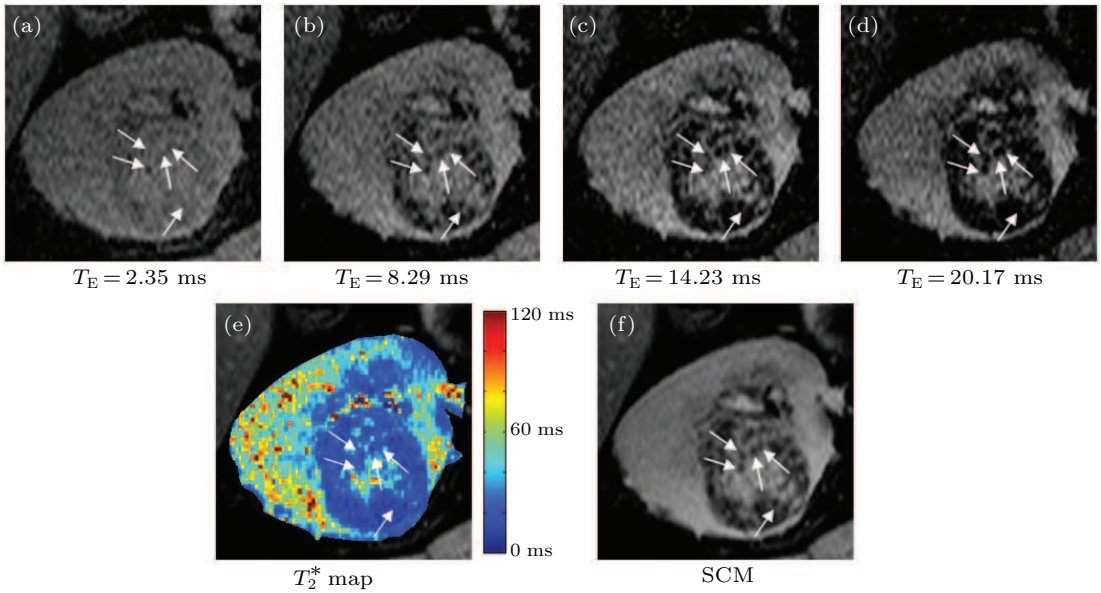


Fig. 6. (color online) Comparison of *in vivo* T_2^*W images, the T_2^* map, and the corresponding SCM of patient #1 who has renal cancer with hemorrhaging. (a)–(d) Representative *in vivo* T_2^*W images at *TE* of 2.35 ms, 8.29 ms, 14.23 ms, and 20.17 ms, respectively. (e) Corresponding T_2^* map. (f) Corresponding SCM generated with normal renal parenchyma as the reference tissue. The white arrows indicate the locations of several dot-like hemorrhages inside the renal cancer.

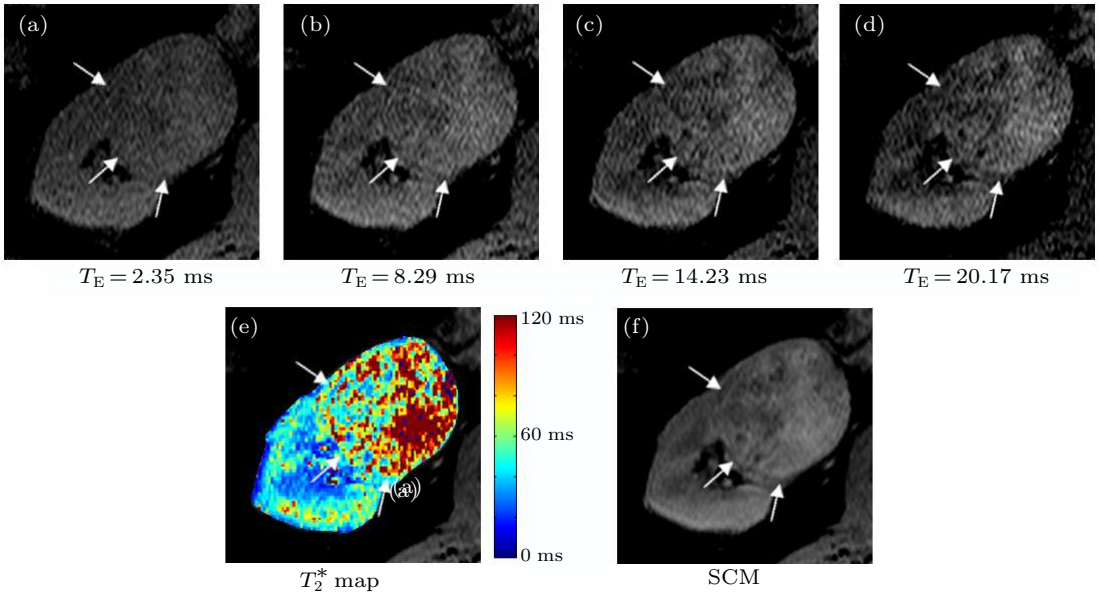


Fig. 7. (color online) Comparison of *in vivo* T_2^*W images, T_2^* map, and the corresponding SCM of patient #2 who has a renal tumor with a pseudocapsule. (a)–(d) Representative *in vivo* T_2^*W images at *TE* of 2.35 ms, 8.29 ms, 14.23 ms, and 20.17 ms, respectively. (e) Corresponding T_2^* map. (f) Corresponding SCM generated with a normal renal parenchyma as the reference tissue. The solid white arrows indicate the pseudocapsule (region of hypointense) of the renal tumor.

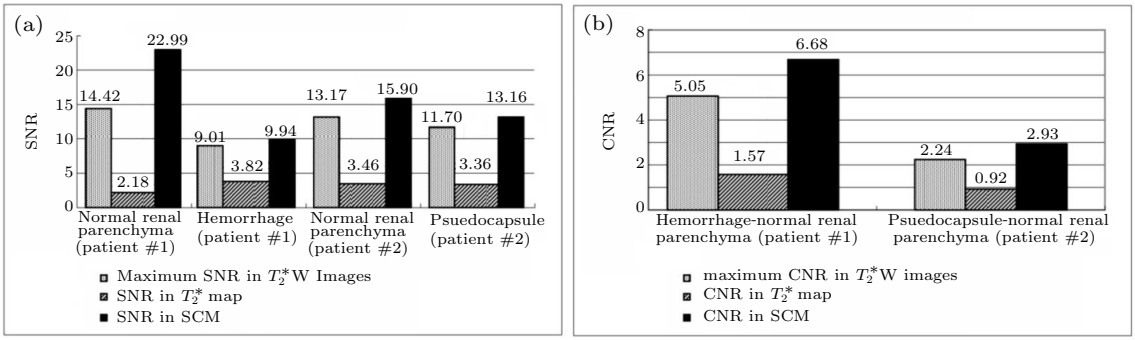


Fig. 8. Comparison of SNRs (and CNRs) in the *in vivo* T_2^*W images that have maximum SNR (and CNR), T_2^* maps, and the corresponding SCMs. (a) Comparison of the SNRs of different tissues (normal renal parenchyma of patient #1, hemorrhage of patient #1, normal renal parenchyma of patient #2, and pseudocapsule of patient #2) in the *in vivo* T_2^*W images that have maximum SNR, T_2^* maps, and the corresponding SCMs. The horizontal axis shows different tissues and the longitudinal axis shows the SNR. (b) Comparison of the CNRs of different pairs of tissues (hemorrhage-normal renal parenchyma, and pseudocapsule-normal renal parenchyma) in the *in vivo* T_2^*W images that have a maximum CNR, T_2^* maps, and the corresponding SCMs. The horizontal axis shows the different pairs of tissues used to calculate CNRs and the longitudinal axis shows the CNR.

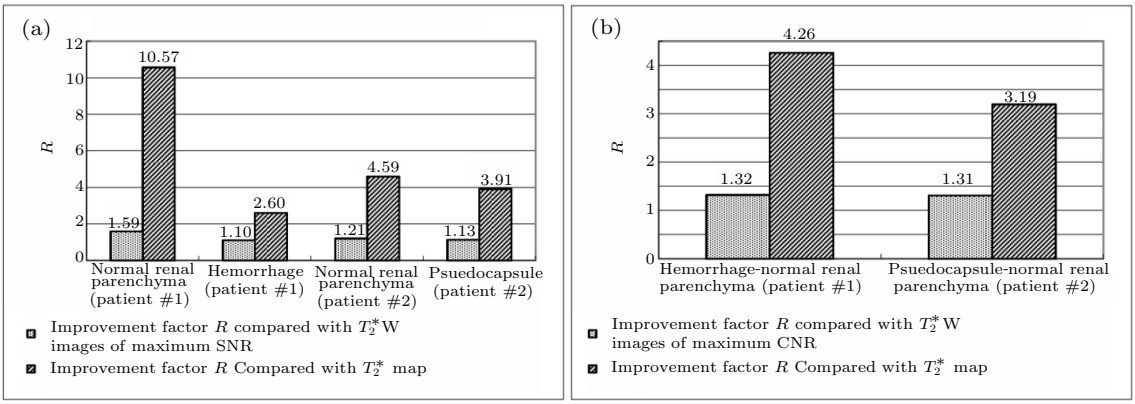


Fig. 9. Comparison of the improvement of SNRs (and CNRs) of different tissues (and pairs of tissues). (a) Comparison of SNR improvement factors (R) of different tissues (normal renal parenchyma of patient #1, hemorrhage of patient #1, normal renal parenchyma of patient #2, and pseudocapsule of patient #2). Improvement factors R of SNR relative to T_2^*W images of maximum SNR and the T_2^* maps are indicated by dotted bars and slashed bars, respectively. The horizontal axis shows different tissues and the longitudinal axis shows the improvement factor R of the SNR. (b) Comparison of the CNR improvement of different pairs of tissues (hemorrhage-normal renal parenchyma, and pseudocapsule-normal renal parenchyma). The improvement factor R of CNR relative to T_2^*W images of maximum CNR and the T_2^* maps are indicated by dotted bars and slashed bars, respectively. The horizontal axis shows different pairs of tissues and the longitudinal axis shows the improvement factor R of CNR.

In Fig. 8, we compare SNRs (and CNRs) in the *in vivo* T_2^*W images that have the maximum SNR (and CNR), the T_2^* maps, and the corresponding SCMs. Figure 8(a) shows the comparison of the SNRs of different tissues (normal renal parenchyma of patient #1, hemorrhage of patient #1, normal renal parenchyma of patient #2, and pseudocapsule of patient #2) in the *in vivo* T_2^*W images that have a maximum SNR, T_2^* maps, and the corresponding SCMs. The horizontal axis shows different tissues and the longitudinal axis shows the SNR. Figure 8(b) shows the comparison of the CNRs of different pairs of tissues (hemorrhage-normal renal parenchyma, and pseudocapsule-normal renal parenchyma) in the *in vivo* T_2^*W images that have a maximum CNR, the T_2^* maps, and the corresponding SCMs. The horizontal axis shows the different pairs of tissues used to calculate the CNRs and the longitudinal axis shows the CNR.

In Fig. 9, we compare the improvement of the SNRs (and CNRs) of different tissues (and pairs of tissues). Figure 9(a) shows the SNR improvement of different tissues (normal renal parenchyma of patient #1, hemorrhage of patient #1, normal renal parenchyma of patient #2, and pseudocapsule of patient #2). The improvement factor R of the SNR relative to T_2^*W images of the maximum SNR and the T_2^* maps are indicated by dotted bars and slashed bars, respectively. The horizontal axis shows different tissues and the longitudinal axis shows the improvement factor R of the SNR. Figure 9(b) shows the CNR improvement of different pairs of tissues (hemorrhage-normal renal parenchyma, and pseudocapsule-normal renal parenchyma). The improvement factor R of the CNR relative to T_2^*W images of a maximum CNR and the T_2^* maps are indicated by dotted bars and slashed bars, respectively. The horizontal axis shows different pairs of tissues and the longitudinal axis shows the improvement factor R of the CNR.

4. Discussion

The importance of accurate morphological evaluation in MRI diagnosis has been well recognized. For renal cancer, previous studies have shown that hemorrhage often implies a poor prognosis.[16,17] On the other hand, a pseudocapsule, which is usually found in the early stages of renal cancer, has been proposed as a sign of a localized intrarenal lesion where partial nephrectomy could be used.[18–21]

The preliminary results of the first simulation study demonstrate that the SCM technique can provide improved morphological evaluation of renal cancers compared to the corresponding T_2^*W MR images and T_2^*maps. As shown in Fig. 2, SCMs (see Figs. 2(g), 2(m), and 2(s)) can reveal small solid circles that are ambiguous or invisible in the corresponding T_2^*W images (see Figs. 2(b)–2(e), 2(h)–2(k), and 2(n)–2(q)) and T_2^*maps (Figs. 2(f), 2(l), and 2(r)). For example, at a noise level of 16%, the small solid circles of bottom series (tissue 3), with radii of 1 and 2 pixels (indicated by white arrows), are invisible in Fig. 2(n) ($T_E = 2$ ms) and ambiguous in Figs. 2(o)–2(q) and 2(r). In contrast, in the corresponding SCM shown in Fig. 2(s), the small circles can be easily identified from the background tissue (tissue 1) and show clear boundaries. Results of the simulation study are strongly supported by the results of the *in vivo* experiments, which demonstrate that the SCM technique can improve the accuracy of the morphological evaluation of hemorrhage and pseudocapsule renal cancer by unveiling fine structures that are ambiguous or even hidden in the original T_2^*W images and the corresponding T_2^* map. For patient #1, as shown in Figs. 6(a)–6(e), no individual T_2^*W image or the corresponding T_2^* map can accurately depict the details of dot-like hemorrhages (indicated by white arrows) of the renal cancer. The ambiguous boundaries of hemorrhages can influence the accurate evaluation of the extent of the hemorrhage. However, these hemorrhage details are precisely presented in the corresponding SCM (see Fig. 6(f)) with clear boundaries. For patient #2, as shown in Figs. 7(a)–7(e), the psuedocapsule is hardly visible in all of the original T_2^*W images and the corresponding T_2^* map. On the contrary, in the corresponding SCM (see Fig. 7(f)), the psuedocapsule is clearly visible (region of hypointense indicated by white arrows).

The improvement in morphological evaluation is due to the improvement in the SNR and CNR by using the SCM technique. Comparisons shown in Fig. 3 imply that the SCM technique can provide much higher SNRs (or CNRs) for all tissues (or pairs of tissues) at different noise levels (4%, 8%, and 16%). For example, at the noise level of 4% (see Figs. 3(a) and 3(d)), the SNR of tissue 1 in the SCM was 75.57, which is approximately 2.47 times the one in the simulated T_2^*W image that gives a maximum SNR (30.53), and 9.6 times the one in the corresponding T_2^* map (7.87). The CNR between tissue 1 and tissue 2 in the SCM was 4.70, which is approximately 2.09 times the one in the simulated T_2^*W image that offers the maximum CNR (2.25), and 1.94 times the one in the corresponding T_2^*map (2.42). Comparisons of the improvement factors of SNR and CNR shown in Fig. 4 illustrate that compared with the simulated T_2^*W images, the improvement factor of the SNR ranges from 1.87 to 2.47 and the improvement factor of the CNR ranges from 2.09 to 2.43. Figure 4 demonstrates that compared with the T_2^* maps, the improvement factor of the SNR ranges from 3.85 to 33.31, and the improvement factor of the CNR ranges from 1.94 to 8.14. It is also shown that for a given noise level, the higher the SNR (or CNR) of the given tissue (or given pair of tissues) in the simulated T_2^*W image is, the higher improvement factor is. For example, at the noise level of 4%, the SNRs in simulated T_2^*W images of tissue 1, tissue 2, and tissue 3 are 30.53, 28.08, and 23.37, respectively, while the improvement factor R relative to T_2^*W images are 2.47, 2.41, and 2.20, respectively, and the improvement factor R relative to T_2^* maps are 9.60, 6.56, and 3.85, respectively. For the noise level of 4%, the CNRs in simulated T_2^* weighted images of tissues 1 and 2, and tissues 1 and 3 are 2.25 and 6.86, respectively, while the improvement factors Rrelative to T_2^*W images are 2.09 and 2.28, respectively, and the improvement factor R relative to T_2^* maps are 1.94 and 3.02, respectively. The *in vivo* experiments clearly confirm these simulation re-

sults. As illustrated by Fig. 8, for each type of tissue (or pairs of tissue), it is evident that the SNRs (or CNRs) in SCMs are much higher than the SNRs (or CNRs) in the corresponding T_2^*W images that have maximum SNRs (or CNRs) and the corresponding T_2^* maps. As shown in Fig. 9, the improvement factors R of the SNR (or CNR) relative toT_2^*W image and T_2^* map depend on the SNR (or CNR) of the original T_2^*W image.

The consistency between the results of the simulation experiment and that of *in vivo* experiment is due to that the signals of multi-echo T_2^*W images in both experiments follow the same rule. In the simulation study, the signal of multi-echo T_2^*W images follows a monoexponential formula given by $I_s(T_E) = \rho \exp(-T_E/T_2^*)$, where ρ is a constant of relative proton density which is set to be 1. For the *in vivo* experiment where an FLASH pulse sequence is implemented, the signal is actually determined not only by the T_2^* effect, but also the T_1 effects and the relative proton density.[38] However, considering the specific MR scanning parameters implemented in the *in vivo* experiment and the characteristics of tissues of interest (hemorrhage, pseudocapsule, and parenchyma), the signal of multiecho T_2^*W images in the *in vivo* experiment can be considered to follow the same rule as the ones in the simulation study. First, for the gradient echo pulse sequence, by utilizing a small flip angle, the T_1 relaxation component is ignorable while the T_2^* effect becomes dominant.[44] Small flip angle excitation disturbs the longitudinal magnetization only slightly. As a consequence, the recovery due to T_1 relaxation is very small and can be ignored.[44] The flip angle implemented in our *in vivo* experiments is 15°, which reduces the longitudinal magnetization by only 3%.[45] Thus, the signals of T_2^*W images in our *in vivo* experiment can be assumed to be independent of T_1 effects and follow the same monoexponential formula as the simulation study. Second, for each patient, the relative proton densities (RPD) of all tissues of interest can be considered as a constant. To evaluate the differences of RPD of different tissues of interest, the RPD values of tissues of interest for each patient have been estimated by fitting a monoexponential model, as described in previous literature.[42] The mean RPD values of hemorrhage and parenchyma of patient #1 are 4.86 ± 0.17 and 4.96 ± 0.08, respectively. The mean RPD values of pseudocapsule and parenchyma of patient #2 are 4.90 ± 0.10 and 5.05 ± 0.09, respectively. The percentage differences of RPD is defined as

$$|\mathrm{RPD}_{\mathrm{tissue1}} - \mathrm{RPD}_{\mathrm{tissue2}}| / [(\mathrm{RPD}_{\mathrm{tissue1}} + \mathrm{RPD}_{\mathrm{tissue2}})/2] \times 100\%,$$

where $\mathrm{RPD}_{\mathrm{tissue1}}$ and $\mathrm{RPD}_{\mathrm{tissue2}}$ denote the relative proton density of tissue 1 and tissue 2 respectively, and $|\ |$ denotes the absolute value. The percentage difference of RPD of hemorrhage and parenchyma (patient #1) is merely 2% The percentage difference of RPD of pseudocapsule and parenchyma (patient #2) is merely 3%. Therefore, for each patient, the RPD of all tissues of interest can be considered as a constant which is similar to the condition of simulation study. According to the analysis above, the signal of multi-echo T_2^*W images in the *in vivo* experiment and the simulation study can be considered to follow the same rule. This is the reason why the results of the *in vivo* experiment are consistent with the first simulation study.

The effects of the number of echoes N on the SCM have also been evaluated. The results of the second simulation study demonstrate that for a fixed total sampling time T_a, more echoes (larger N) leads to a higher SNR/CNR, which can be achieved in an SCM. As shown in Figs. 5(a) and 5(b), the quantitative comparisons of the SNRs (and CNRs) of these SCMs illustrate that the more the echoes are used to generate SCMs, the higher the SNR/CNR of the SCMs are. For instance, for $N = 12$, the SNR of tissue 1 in the SCM was 24.16, which is higher than the ones in the SCM generated from 6 echoes (22.14) and 3 echoes (21.12). The CNR between tissue 1 and tissue 2 in the SCM with $N = 12$ was 1.24, which is higher than the one in the SCM with $N = 6$ (1.23), and the one in the SCM with $N = 3$ (1.14). For practical application, it is well known that T_s is inversely proportional to the receiver bandwidth (BW).[38] For a given T_a, if N increases, the corresponding T_s will shorten and the BW will increase. For a given field of view (FOV), BW is proportional to the readout gradient G_r ($\mathrm{BW} = \gamma G_r \mathrm{FOV}_r$), where γ is the gyromagnetic ratio, and the FOV_r is the FOV in readout direction.[38] For a fixed FOV and a fixed spatial resolution, if the BW increases, the readout gradient G_r should also be increased. However, the maximum G_r is limited by the hardware of the MR scanner. Therefore, for a given T_a, the maximum number of echoes that can be obtained is limited by the maximum G_r that the MR scanner can provide. All in all, in clinical application, for a fixed total sampling time T_a, one should increase the number of echoes as much as possible to achieve better SNRs and CNRs in an SCM.

One weakness of this study is the limited number of patients. We are actively working with physicians to increase the number of patients for clinical applications of SCMs in a typical clinical setting. Furthermore, in this study, the SCM technique is applied to the T_2^*W MR imaging of a kidney only. Although it is out of the scope of this study, the SCM technique could easily be extended to other organs such as the liver or prostate. SCMs can additionally be applied to other MR imaging techniques such as T_1 weighted imaging, T_2 weighted imaging, and perfusion weighted imaging (PWI), which have also been widely used in assessment of renal cancers.

5. Conclusion

In conclusion, our preliminary results have demonstrated that the SCM technique can improve the morphological evaluation of hemorrhages and pseudocapsules in renal cancer through improvements in SNR and CNR. Moreover, for a given total sampling time, more echoes are used to generate the SCM, and higher SNRs and CNRs can be achieved.

Appendix A: Comparison of TSM and SCM

A simulation experiment has been conducted in this appendix to compare the sensitivity to choice of reference tis-

sue of a TSM with the one of an SCM. The phantom implemented in this simulation consists of three tissues with different T_2^* values (10, 20, and 45 ms for tissue A, tissue B, and tissue C, respectively) as shown in Fig. A1(a). The 12-echo T_2^*W images are generated at T_E ranging from 2 to 24 ms at an interval of 2 ms using a mono exponential model $I_s(T_E) = \rho \exp(-T_E/T_2^*)$, where T_E denotes the echo time, I_s denotes the signal intensity at T_E, ρ denotes relative proton density which is set to be 1. TSMs and the corresponding SCMs generated with different reference tissues (tissue A, tissue B, and tissue C, respectively) have been compared with each other in Fig. A1. The contrast between tissue A and tissue C is calculated by

$$\text{Contrast}_{A-C} = |I_{sA} - I_{sC}|/[(I_{sA} + I_{sC})/2],$$

where I_{sA} and I_{sC} are signal intensities of tissue A and C, respectively.

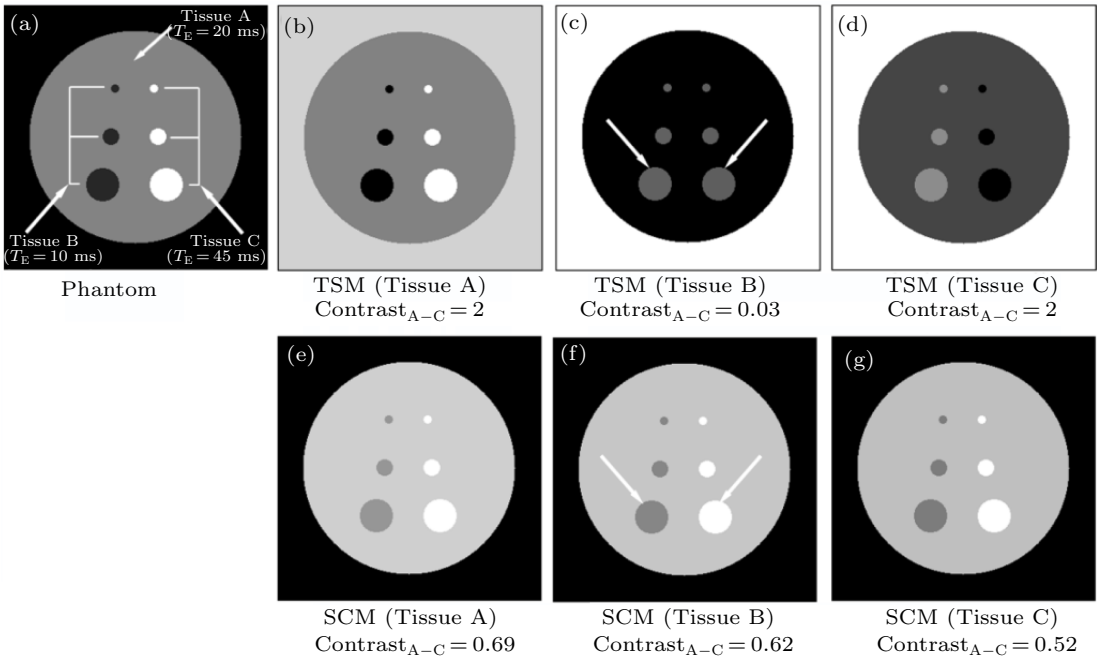


Fig. A1. Comparison of TSM and SCM. (a) Phantom composed of three tissues with different T_2^* values (10, 20, and 45 ms for tissue A, tissue B, and tissue C). (b)–(d) TSMs generated with different reference tissues (tissues A, B, and C). (e)–(g) Corresponding SCMs generated with different reference tissues. The contrasts beneath TSMs and SCMs denote the contrasts between tissue A and tissue C in the corresponding TSM or SCM.

As shown in Fig. A1, compared with TSM, SCM is less sensitive to the choice of reference tissue. For different reference tissues, the Contrast$_{A-C}$ in TSMs ranges from 0.03 to 2, while the Contrast$_{A-C}$ in SCMs ranges from 0.52 to 0.69. What is more, in the TSM generated with Tissue B as reference tissue (see Fig. A1(c)), it is hard to distinguish tissue A ($T_2^* = 10$ ms) from tissue C ($T_2^* = 45$ ms) since they have similar MSE to tissue B and therefore have a low contrast between them (Contrast$_{A-C} = 0.03$). On contrary, in the corresponding SCM (see Fig. A1(f)), it is easy to distinguish tissue A and tissue C, and the contrast between tissue A and tissue C is 0.62 which is about 20 times the one in the corresponding TSM which is merely 0.03.

In summary, the results of this experiment suggest that compared with a TSM the SCM is less sensitive to the choice of reference tissue which makes it a more reliable method. If the reference tissue is not properly selected, the TSM technique could fail to provide enough contrast between tissues of interest (see Fig. A1(c)). Conversly, for different reference tissues, SCMs can always provide enough contrast between tissues of interest (see Figs. A1(e)–A1(g)).

References

[1] Society A C 2012 *Cancer Facts and Figures* (Atlanta: American Cancer Society)
[2] Kamel I R, Hochman M G, Keogan M T, Eng J, Longmaid H E, Dewolf W and Edelman R R 2004 *J. Comput. Assist. Tomogr.* **28** 327
[3] Harmon W J, King B F and Lieber M M 1996 *J. Urol.* **155** 863
[4] Takahashi S, Ueda J, Furukawa T, Higashino K, Tsujihata M, Itatani H, Narumi Y and Nakamura H 1996 *J. Comput. Assist. Tomogr.* **20** 863
[5] Han X N, Peng L R, Liu G H and Wang J 2005 *Chin. J. Med. Imag. Technol.* **21** 776
[6] Adey G S, Pedrosa I, Rofsky N M, Sanda M G and Dewolf W C 2008 *Urology* **71** 47
[7] Ramchandani P, Soulen R L, Schnall R I, Seidmon E J, Friedman A C, Radecki P D and Caroline D F 1986 *Urology* **27** 564
[8] Amendola M A, King L R, Pollack H M, Gefter W, Kressel H Y and Wein A J 1990 *Cancer* **66** 40
[9] Reznek R H 1996 *Eur. Radiol.* **6** 120
[10] Russo P 2000 *Semin. Oncol.* **27** 160
[11] Heidenreich A and Ravery V 2004 *World J. Urol.* **22** 307
[12] Spero M, Brkljacic B, Kolaric B and Marotti M 2010 *Clin. Imaging* **34** 441
[13] van der Veldt A A M, Meijerink M R, van den Eertwegh A J M and Boven E 2010 *Target. Oncol.* **5** 95
[14] Prasad P V, Edelman R R and Epstein F H 1996 *Circulation.* **94** 3271
[15] Tanaka Y O, Anno I, Itai Y and Abe T 1993 *J. Comput. Assist. Tomogr.* **17** 749
[16] Mcclennan B L and Deyoe L A 1994 *Radiol. Clin. N. Am.* **32** 55
[17] Kim J K, Kim T K, Ahn H J, Kim C S, Kim K R and Cho K S 2002 *Am. J. Roentgenol.* **178** 1499

[18] May M, Brookman-Amissah S, Roigas J, Gilfrich C P, Pflanz S, Hoschke B and Gunia S 2010 *Urol. Oncol.-Semin. Orig. Investig.* **28** 274
[19] Jeong I G, Jeong C W, Hong S K, Kwak C, Lee E and Lee S E 2006 *Urology* **67** 709
[20] Klatte T, Chung J, Leppert J T, Lam J S, Pantuck A J, Figlin R A and Belldegrun A S 2007 *BJU Int.* **99** 821
[21] Cho H J, Kim S J, Ha U S, Hong S H, Kim J C, Choi Y J and Hwang T K 2009 *Eur. Urol.* **56** 1006
[22] Saha P K and Udupa J K 2001 *IEEE Trans. Med. Imaging* **20** 1140
[23] Placidi G, Alecci M and Sotgiu A 2003 *Phys. Med. Biol.* **48** 1987
[24] Gerig G, Kubler O, Kikinis R and Jolesz F A 1992 *IEEE Trans. Med. Imaging* **11** 221
[25] Zu Z L, Zhou K, Zhang S G, Gao S and Bao S L 2008 *Chin. Phys. B* **17** 328
[26] Schabel M C and Parker D L 2008 *Phys. Med. Biol.* **53** 2345
[27] Saritas E U, Lee J H and Nishimura D G 2011 *IEEE Trans. Med. Imaging* **30** 424
[28] Reeder S B, Herzka D A and Mcveigh E R 2004 *Magn. Reson. Med.* **52** 123
[29] Halse M, Rioux J, Romanzetti S, Kaffanke J, Macmillan B, Mastikhin I, Shah N J, Aubanel E and Balcom B J 2004 *J. Magn. Reson.* **169** 102
[30] Shapiro M D 2006 *Magnetic Resonance Imaging Clinics of North America* **14** 97
[31] Hutton C, Josephs O, Stadler J, Featherstone E, Reid A, Speck O, Bernarding J and Weiskopf N 2011 *Neuroimage* **57** 101
[32] Greenman R L, Shirosky J E, Mulkern R V and Rofsky N M 2003 *J. Magn. Reson. Imaging* **17** 648
[33] Fushimi Y, Miki Y, Urayama S I, Okada T, Mori N, Hanakawa T, Fukuyama H and Togashi K 2007 *Eur. Radiol.* **17** 2921
[34] Debatin J 2004 *Rofo-Fortschr. Gebiet Rontgenstrahlen Bildgeb. Verfahr.* **176** 787
[35] Haacke E M, Li M and Juvvigunta F 2011 *International Society for Magnetic Resonance in Medicine* May 7-13, 2011 Montréal, Québec, Canada
[36] Li M, Bashir A, Yu Y, Xuan Y, Latif Z, Garbern J, Hu J and Haacke E M 2010 *International Society for Magnetic Resonance in Medicine* May 1-7, 2010 Stockholm, Sweden
[37] Haacke E M, Li M and Juvvigunta F 2012 *Magn. Reson. Imaging*
[38] Haacke E M, Brown R W, Thompson M R and Venkatesan R 1999 *Magnetic Resonance Imaging : Physical Principles and Sequence Design* (New York: John Wiley & Sons)
[39] Coupe P, Manjon J V, Gedamu E, Arnold D, Robles M and Collins D L 2010 *Med. Image Anal.* **14** 483
[40] Hashemieh M, Azarkeivan A, Akhlaghpoor S, Shirkavand A and Sheibani K 2012 *Archives of Iranian Medicine* **15** 91
[41] Henninger B, Kremser C, Rauch S, Eder R, Zoller H, Finkenstedt A, Michaely H J and Schocke M 2012 *Eur. Radiol.* **22** 2478
[42] Hatabu H, Alsop D C, Listerud J, Bonnet M and Gefter W B 1999 *Eur. J. Radiol.* **29** 245
[43] Correia M M, Newcombe V F J and Williams G B 2011 *Neuroimage* **57** 1103
[44] Chavhan G B, Babyn P S, Thomas B, Shroff M M and Haacke E M 2009 *Radiographics* **29** 1433
[45] Elster A D 1993 *Radiology* **186** 1